Journal of Nanobiotechnology

RESEARCH

Open Access

Macrophage-derived mitochondria-rich extracellular vesicles aggravate bone loss in periodontitis by disrupting the mitochondrial dynamics of BMSCs

Jiayin Yan[1,2,3,4], Tian Yang[1,2,3], Siyuan Ma[1,2,3], Danfeng Li[1,2,4], Cheng Hu[1,2,4] and Jiali Tan[2,4*]

Abstract

Background Periodontitis is the leading cause of tooth loss in adults due to progressive bone destruction, which is closely related to the dysfunction of bone mesenchymal stem cells (BMSCs). Existing evidence suggests that mitochondrial disorders are associated with periodontitis. However, whether mitochondrial dysregulation contributes to the osteogenic impairment of BMSCs and the underlying mechanisms remain unclear. Macrophages have been shown to communicate extensively with BMSCs in periodontitis. Recent studies have reported a novel manner of cellular communication in which mitochondria-rich extracellular vesicles (MEVs) transfer mitochondria from parent cells to recipient cells, playing a role in both physiological and pathological conditions. Therefore, we aimed to investigate the role of MEVs in orchestrating the crosstalk between macrophages and BMSCs in periodontitis to formulate management strategies for bone loss.

Results Our results revealed that macrophages underwent significant mitochondrial dysfunction and inflammation in periodontitis and that MEVs derived from these macrophages played a role in alveolar bone destruction. Furthermore, cell imaging showed that inflammatory macrophages packaged numerous damaged mitochondria into MEVs, and the entry of these impaired mitochondria into BMSCs disrupted mitochondrial dynamics and hindered donut-shaped mitochondria formation, leading to osteogenic dysfunction. Proteomic analysis revealed that the proteins enriched in macrophage-derived MEVs were largely related to mitochondria and the formation and transport of vesicles. Additionally, we found that MEVs from macrophages significantly increased lipocalin 2 (LCN2) in BMSCs in periodontitis and that LCN2 perturbed mitochondrial morphological changes in BMSCs by inducing the degradation of OMA1 and accumulation of OPA1, resulting in osteogenesis impairment in BMSCs. Inhibition of LCN2 rescued the osteogenic dysfunction of BMSCs and alveolar bone loss in periodontitis.

Conclusions The transfer of mitochondria to BMSCs via MEVs exacerbates alveolar bone resorption through LCN2/OMA1/OPA1 signaling in periodontitis. Inhibition of LCN2 alleviates inflammatory bone loss, suggesting a promising therapeutic strategy for periodontitis.

Keywords Periodontitis, Bone mesenchymal stem cells, Macrophages, Mitochondrial dynamics, Lipocalin 2

*Correspondence:
Jiali Tan
tanjiali@mail.sysu.edu.cn
Full list of author information is available at the end of the article

Graphical Abstract

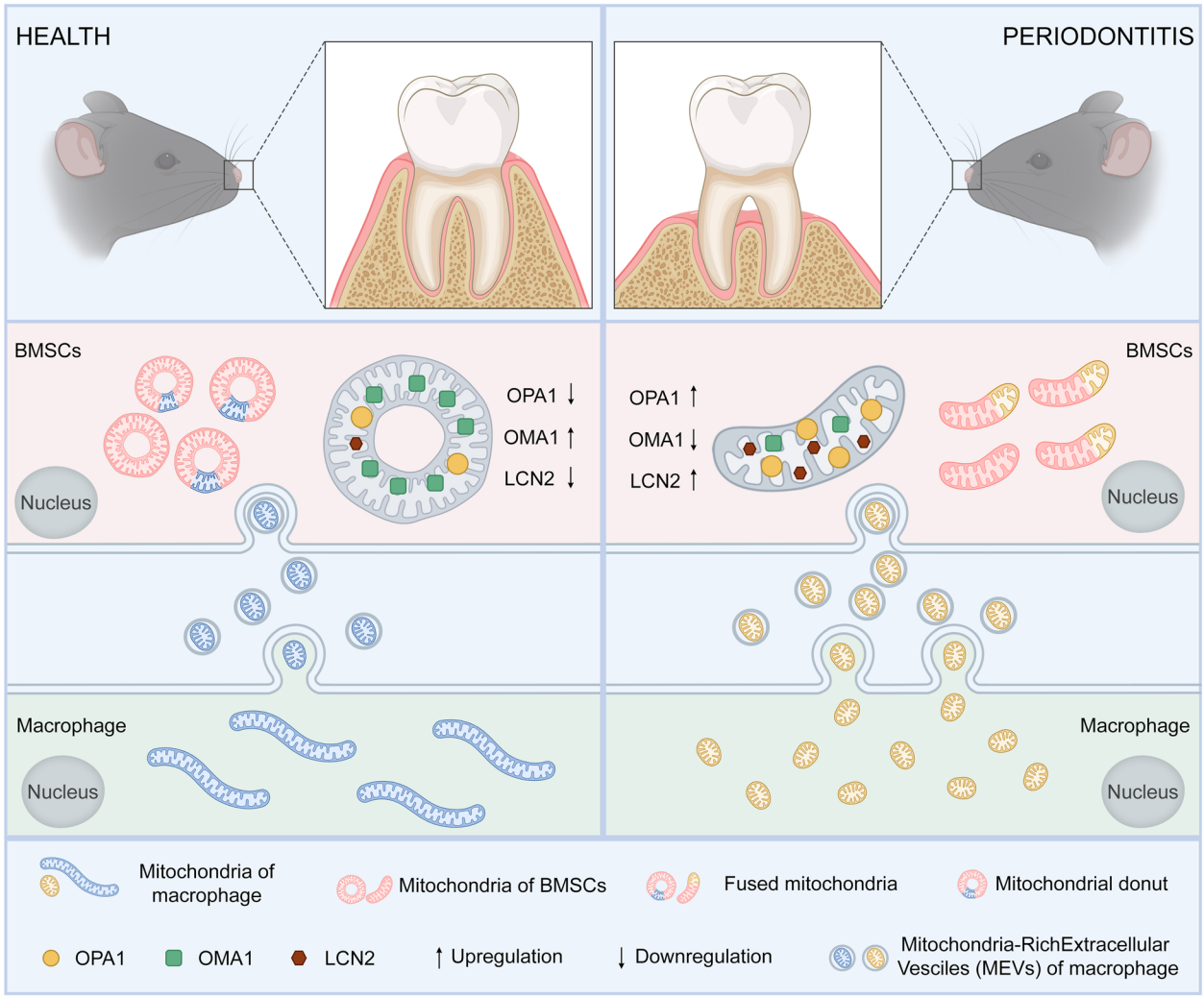

Background

Periodontitis, the leading cause of tooth loss in adults, is characterized by progressive inflammatory bone destruction, with *Porphyromonas gingivalis* (*P.g*) as a key pathogen [1]. However, no efficient strategies have been approved for treating inflammatory alveolar bone loss in periodontitis because of the limited understanding of the underlying mechanisms [2, 3]. Bone mesenchymal stem cells (BMSCs) are the primary source of osteoblasts in alveolar bone, and play broad roles in maintaining homeostasis and repairing periodontal supporting tissue [4]. In the inflammation process of periodontitis, prolonged stimulation by various virulence factors significantly hinders the osteogenic activity of BMSCs and the proportion of osteogenic lineage cells derived from BMSCs [5]. This reduction does not recover even after periodontal treatment, leading to persistent bone loss and difficulties in repair [5]. However, the specific mechanisms of BMSC dysfunction in periodontitis are still unexplored [6]. Elucidating these mechanisms and developing targeted therapeutic strategies for inflammatory bone loss are highly important.

Recently, studies have reported that various periodontal cells from patients with chronic periodontitis exhibit mitochondrial disorders, including a reduction in the mitochondrial membrane potential, decreased cellular oxygen consumption, and increased reactive oxygen species (ROS) [7, 8]. These findings suggest that mitochondrial dysregulation may be a significant event in periodontitis [9]. Mitochondria are commonly known

as the powerhouses of cells, but recent studies have shown that, under osteogenic conditions, they also function in the biomineralization process [10, 11]. Calcium phosphate biomineral precursors, which are formed in mitochondria, are secreted extracellularly through mitochondria-derived vesicles or mitophagy, facilitating the mineralization of collagen fibers and promoting osteogenic maturation [11]. This process is based on the morphological changes driven by mitochondrial dynamics, with the downregulation of optic atrophy 1 (OPA1), a dynamin superfamily protein that controls the fusion and remodeling of the inner mitochondrial membrane and cristae, resulting in donut-shaped mitochondria [12]. Disruption of mitochondrial dynamics hinders mitochondrial donut formation, thereby triggering biomineralization dysfunction and impaired osteogenesis [12]. However, whether the impaired osteogenesis of BMSCs in periodontitis is associated with the dysregulation of mitochondrial dynamics is poorly understood.

Macrophages, the main effector cells of the innate immune system, constitute the first line of defense against periodontal pathogens, causing inflammatory damage to periodontal tissues [13]. In periodontitis, the permeability of the periodontal epithelium facilitates extensive communication between macrophages and BMSCs [14–16]. Extracellular vesicles (EVs) serve as broad media for intercellular communication and may also play a role in this process [17]. Macrophages release EVs under both physiological and pathological conditions; encapsulate lipids, nucleic acids, and proteins from parent cells; and regulate the functions of target cells [18]. Recently, studies have shown that EVs containing mitochondria (mitochondria-rich EVs, MEVs) deliver mitochondria to recipient cells, thereby regulating the physiology and function of various organ systems in both health and disease [19, 20]. For example, adipocytes transfer impaired mitochondria via MEVs to cardiomyocytes for processing, thereby protecting cardiomyocytes from stress; macrophages transfer mitochondria via MEVs to sensory neurons for deliberate resolution of inflammatory pain [21, 22]. However, the effects and mechanisms of multicellular communication via MEVs in periodontitis remain unclear.

Herein, we aimed to investigate the role of MEVs in orchestrating the crosstalk between macrophages and BMSCs in periodontitis-induced bone loss. We examined the transfer of mitochondria from macrophages to BMSCs via MEVs both in vivo and in vitro, which inhibited the osteogenesis of BMSCs and exacerbated bone loss in periodontitis. Furthermore, we found that MEVs from inflammatory macrophages hindered the formation of donut-shaped mitochondria in BMSCs in periodontitis. Additionally, the protein profile of MEVs from macrophages, before and after infection with *P.g*, was mapped, and we determined that the mitochondrial-related protein lipocalin 2 (LCN2) was crucial. Subsequent experiments confirmed that MEVs from macrophages significantly increased LCN2 levels in BMSCs in periodontitis. The overexpression of LCN2 disturbed mitochondrial dynamics and inhibited the formation of mitochondrial donuts in BMSCs by inducing the degradation of OMA1 zinc metallopeptidase (OMA1) and the accumulation of OPA1. Inhibition of LCN2 rescued the osteogenic dysfunction of BMSCs and alveolar bone loss in periodontitis, suggesting a promising therapeutic strategy for periodontitis.

Materials and methods

Cell cultures

To isolate BMSCs, mice (4-week-old male, C57BL/6) were anesthetized with isoflurane and then euthanized. The femurs and tibias were cut and flushed. The cells were cultured and passaged to the second generation at 37 °C with 5% CO_2.

To isolate macrophages, bone marrow cells were treated with RBC lysis buffer (Sigma, STL, USA). The cells were seeded for 24 h, and nonadherent cells were harvested and cultured with 25 ng/mL M-CSF (Novoprotein, Jiangsu, China) for 7 days.

Bacterial strains and cultures

Porphyromonas gingivalis (*P.g*, ATCC 33277) was cultured in brain heart infusion broth supplemented with 1 μg/mL vitamin K in an anaerobic tank (80% N_2, 10% H_2, and 10% CO_2) as previously described [23]. Bacterial counts were performed via spectrophotometry (OD600 nm of 0.5 = 10^8 cells/mL).

Inflammatory macrophage models and extraction of MEVs

The macrophages were infected with *P.g* for 1 h at a multiplicity of infection (MOI) of 100 (*P.g*-Mϕ) [24, 25]. After infection, the cells were washed with PBS and incubated with 0.3 mg/mL gentamycin (Sigma, STL, USA) and 6 mg/mL metronidazole (APExBio, Houston, USA) for 1 h [24, 25]. Uninfected cells were used as controls (Con-Mϕ). All culture media and PBS were filtered through a 0.1 μm filter (Millipore, Massachusetts, USA). The conditioned medium was collected, and after centrifugation at 4 ℃ [17], Con-MEVs or *P.g*-MEVs were obtained (Fig. 1A). BMSCs were incubated with MEVs (2.67×10^8/mL) for subsequent experiments.

Quantitative RT–PCR

Total RNA was isolated via TRIzol. Complementary DNA (cDNA) was synthesized via the HiScript II Q RT SuperMix Kit, according to the manufacturer's protocol

(Vazyme, Nanjing, China). Table S1 lists the sequences of the primers used. Quantitative RT–PCR was performed in triplicate with a LightCycle96 using FastStart Essential DNA Green Master Mix (Roche, Basel, Switzerland). The 2-ΔΔCT method was used to analyze the results.

Measurement of particle size and concentration

The particle size and concentration of the MEVs were determined via a NanoSight NS300 analyzer (Malvern Panalytical, Melvern, USA). The pellets were resuspended and detected with a 405 nm laser. Nanoparticle tracking analysis (NTA) was performed with PBS as a control to determine the appropriate camera level and detection threshold.

Flow cytometry analysis

Flow cytometry analysis was performed to detect the proportions of total mitochondria and undamaged mitochondria in MEVs [26]. The particles were stained with MitoTracker Green or MitoTracker Deep Red (MTG or MTDR; Thermo Fisher Scientific, #M22426 or #M7514; Waltham, USA) at 37 °C for 30 min. The immunophenotype of the MEVs was characterized with CD29 and CD63 (1:200, BioLegend, #101211 and #123107; California, USA), and the particles were labeled with antibodies for 30 min at 4 °C.

To characterize the specific surface antigens of the macrophages, the cultured cells were blocked with antibodies against CD16/32 (Elabscience, #F0997A; Wuhan, China) and then stained with antibodies against CD11b and F4/80 (1:200, BioLegend, #102207 and #143907) in the dark for 60 min. Unstained cells were used to adjust the voltage. FACS analysis was performed using a BD LSRFortessa (BD, New Jersey, USA).

Transmission electron microscopy (TEM)

For TEM analysis, pellets were fixed in 2.5% glutaraldehyde overnight, then with osmium tetroxide, dehydrated in ethanol, and infiltrated with acetone. Sections were cut via an EM UC7 ultramicrotome (Leica, Wetzlar, Germany), mounted on Formvar-coated grids, and stained with 2% uranyl acetate. Images were obtained with a JEOL JEM-1200EX TEM at 80 kV [27].

Animals

Periodontitis was induced by ligation and *P.g* application. Orthodontic stainless steel ligature wires (0.25 mm) were inserted from the palatal side of the second molar of 3-month-old male C57BL/6 mice. Every 4 days, the mice were injected with 100 μL of MEVs at a concentration of 2.67×10^{10}/mL via tail vein (IV, intravenous injection). The mice were randomly assigned to five groups: Control, Periodontitis, Periodontitis + PBS, Periodontitis + Con-MEVs, and Periodontitis + *P.g*-MEVs. According to the Resource Equation Approach, there were 6 mice in each group [28].

Detection of mitochondrial transfer in vivo

MEVs were stained with 100 nM MitoTracker Red at 37 °C for 30 min and then washed with PBS three times to eliminate the dyes. The labeled MEVs (100 μL, 2.67×10^{10}/mL) were injected into the mice. At 4 h or 24 h post injection, the mice were euthanized, and the hearts were perfused. The heart, liver, spleen, lungs, kidneys and maxilla were separated. Fluorescence was detected via an IVIS Spectrum system (PerkinElmer, Waltham, USA). Maxillae were cryosectioned to assess mitochondrial distribution and then stained with anti-SCA1 (1:200, Abcam, #109211, Waltham, USA) and DyLight 488 secondary antibodies, with DAPI for nuclei.

Micro-computed tomography (Micro-CT)

Micro-CT scanning of the maxillae was performed (μCT 50; SCANCO, Switzerland) with a resolution of 9 μm and parameters of 70 kV and 114 mA. The DataViewer (SR Research, Mississauga, CA) was utilized for 3-dimensional reconstruction. The distance from the cementoenamel junction (CEJ) to the alveolar bone crest (ABC) was measured as the mean value of 4 sites (distal region of the distal buccal root and palatal root of the first molar, and mesial region of the mesial buccal root and palatal root of the second molar). The threshold used for the Micro-CT data evaluation was 2000–10,000 Hu.

Histological staining

The maxillae were decalcified, dehydrated, and embedded in paraffin before being sectioned. They were

(See figure on next page.)

Fig. 1 Macrophages release mitochondria-rich extracellular vesicles (MEVs), and inflammatory macrophages package more damaged mitochondria into MEVs. **A** Macrophage-conditioned media were collected, and cellular debris was excluded by centrifugation at 2000×*g* for 10 min. Subsequent centrifugation at 20,000×*g* for 30 min was performed to isolate the MEVs. MEVs from macrophages treated with PBS served as a control (Con-MEVs), and those from macrophages treated with *Porphyromonas gingivalis* (*P.g*) were designated *P.g*-MEVs. **B** Representative images of nanoparticle tracking analysis (NTA) for MEVs, with the horizontal axis representing diameter (nm) and the vertical axis representing particle concentration (10^6/mL). **C** Representative transmission electron microscopy (TEM) images of MEVs. **D**, **E** The expression of the surface markers CD29 and CD63 on MEVs was tested via flow cytometry. **F**, **G** The contents of mitochondria (MTG) and undamaged mitochondria (MTDR) within MEVs were tested by flow cytometry. Values were mean ± SD, n = 3. *$P \le 0.05$, ***$P \le 0.001$

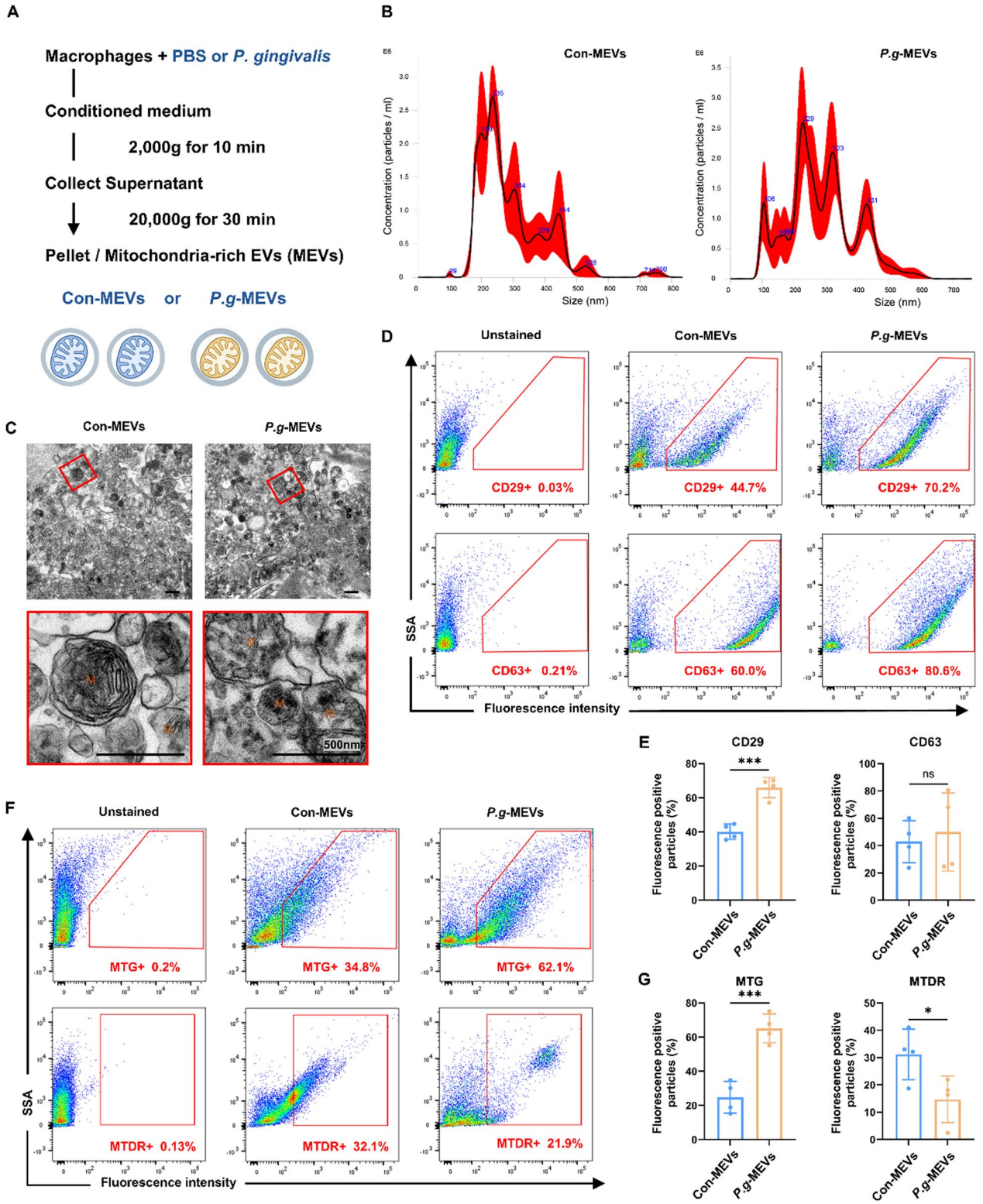

Fig. 1 (See legend on previous page.)

deparaffinized in xylene and rehydrated in graded ethanol before being stained with H&E and Masson's trichrome by staining kits (Solarbio, Beijing, China). The sections were scanned and photographed using a slide scanner (Leica Aperio AT2, Wetzlar, Germany). For immunohistochemistry (IHC) staining, the sections were stained with an anti-LCN2 antibody or anti-RUNX2 antibody (1:200, Abcam, #318209, #192256), followed by secondary antibodies. The mean optical density (MOD) was analyzed via a scanning microscope. Multiple fields of view were taken to calculate the average MOD.

Mitochondrial transfer coculture models

MEVs were collected from macrophages labeled with MitoTracker (green). The BMSCs were preliminarily stained with MitoTracker (red) and Hoechst. Then, the BMSCs were incubated with resuspended MEVs for 24 h, and detected with a Zeiss LSM980 Airyscan confocal microscope.

Alizarin red S (ARS) staining

The culture medium was removed, and 4% formaldehyde was added at room temperature. After being washed three more times, the cells were incubated with ARS staining solution in the dark for 30 min. Then, the formation of mineralized nodules was detected with a microscope.

Immunofluorescence

The cells were stained with MitoTracker (green), and subsequently fixed with 4% formaldehyde. Then, the cells were permeabilized, blocked with 3% BSA containing 0.3% Triton X-100 for 20 min, and incubated with primary antibodies (LCN2, 1:200; Abcam, #318209) and secondary antibodies (Proteintech, #SA00013; Guangzhou, China). Confocal images were acquired with a confocal microscope.

ATP measurement

The level of intracellular ATP was determined with an ATP Assay Kit (Invitrogen, California, USA). After cell lysis, the mixture was harvested and centrifuged at 12,000×*g* for 10 min. Then, the supernatant and luminescence test solution were collected, and ATP determination was performed.

Western blot

Proteins were loaded on 4–12% Bis–Tris gels (GenScript, Piscataway, USA) and transferred to polyvinylidene fluoride membranes (Millipore, USA). After blocking with 5% BSA, the membranes were incubated with primary antibodies (LCN2, 1:1000, Abcam, #ab318209; OPA1, 1:1000, Abcam, #ab42364; OMA1, 1:1000, Affinity, #DF12435; β-actin, 1:10,000, Affinity, #AF7018, Jiangsu, China). After treatment with secondary antibodies, visualization was performed with a ChemiDoc Western ECL system (Bio-Rad, Hercules, USA).

Proteomic analysis of MEVs

MEVs were isolated and dissolved in lysis buffer containing 8 M urea, 1 mM protease inhibitors, and 2 mM EDTA. After centrifugation at 14,000×*g* for 20 min, the supernatant was collected and digested with trypsin. The samples were quenched with formic acid, and LC–MS/MS analysis was performed on a NanoElute UHPLC instrument and timsTOF Pro (Bruker Daltonics, Billerica, USA). The instruments were run for peptide identification and quantification via the DIA method, via the UniProt-proteome_UP000000589_Mus_musculus.fasta database. The Gene Ontology (GO), euKaryotic Ortholog Groups (KOG), and Kyoto Encyclopedia of Genes and Genomes (KEGG) annotations and enrichment analyses were based on the UniProt database. The significant differentially expressed proteins (DEPs) with a fold change >1.5 or <0.6667 and a *P*-value < 0.05 were identified. The R Bioconductor package DESeq2 version 1.40.2 was used to analyze the DEPs.

LCN2-overexpressing BMSC generation

LCN2-overexpressing BMSCs were generated via transduction with a lentiviral vector carrying the LCN2 gene (Genechem, Shanghai, China). The cDNA of LCN2 (available at https://www.ncbi.nlm.nih.gov/nuccore/BC132071.1) was amplified from 293T cells and cloned and inserted into the Ubi-MCS-3FLAG-SV40-puromycin vector. The Ubi-MCS-3FLAG-SV40-puromycin empty vector was used as a negative control (NC). BMSCs were infected with a lentivirus encoding gcGFP (Ubi-MCS-3FLAG-CBh-gcGFP-IRES-puromycin) to determine the optimal MOI. BMSCs were incubated with lentivirus and polybrene for 16 h. After culture in fresh medium for 72 h, positive cells were selected with puromycin. The transduction efficiency was determined by Western blotting and qRT–PCR. The cells transfected with the LCN2 lentivirus mixture were named LCN2^{Hi}, and the cells transfected with the control lentivirus mixture were termed NC.

Statistical analysis

All the data were expressed as the means ± SD. When the data were normally distributed, an unpaired Student's *t*-test was used for two-group comparisons, and analysis of variance (ANOVA) was used for three or more groups, followed by Tukey's Kramer test for multiple comparisons. When the data were not normally distributed, the Mann–Whitney *U* test was applied for

two-group comparisons, and the Kruskal–Wallis H test was applied for three or more groups. Significance was set at a P-value < 0.05 ($^{*}P < 0.05$, $^{**}P < 0.01$, $^{***}P < 0.001$ and $^{****}P < 0.0001$). Statistical analyses were performed with commercial software (GraphPad Prism 9).

Results

Inflammatory macrophages release more damaged mitochondria into MEVs

The identification of macrophages was confirmed by flow-cytometric analysis, with macrophages expressing CD11b (93.9%) and F4/80 (94.2%), indicating that the cells possessed macrophage characteristics (Fig. S1A). To construct inflammatory macrophage models characteristic of periodontitis, we utilized *P.g*, a key periodontal pathogen, to infect macrophages. After infection, the expression of the inflammatory markers *Il-1β*, ***TNF-α,*** *Il-6*, and *Nos2* was significantly increased in macrophages (Fig. S1B). In addition, we found that the mitochondria in infected macrophages were damaged, characterized by a fragmented morphology, a lower membrane potential, and more reactive oxygen species, further confirming the successful creation of inflammatory macrophages in periodontitis (Fig. S2).

Next, the Con-MEVs and *P.g*-MEVs from the macrophages were isolated and characterized. As shown in Fig. 1B, the particle size of the purified MEVs ranged from 100 to 600 nm. The average diameters of the Con-MEVs and *P.g*-MEVs were 277.6 and 264.4 nm, respectively, with no significant difference between them (Fig. 1B, Fig. S3). TEM confirmed that the MEVs were spherical extracellular vesicles, with a number of them containing mitochondria (Fig. 1C). The diameter of the mitochondria-containing vesicles was greater than that of the vesicles without mitochondria (Fig. 1C). Additionally, MEVs reportedly express the biomarkers CD29 and CD63 [26]. Flow cytometry assays demonstrated that both the Con-MEVs and *P.g*-MEVs tested positive for CD29 and CD63. However, the frequency of CD29 was greater in *P.g*-MEVs than in Con-MEVs (Fig. 1D, E).

MTG labels total mitochondria, and MTDR labels functional mitochondria [26]. Therefore, the contents of mitochondria and undamaged mitochondria in MEVs were detected via the MTG and MTDR, respectively. Compared with Con-MEVs, *P.g*-MEVs presented more MTG-positive particles and fewer MTDR-positive particles (Fig. 1F, G). These findings suggest that macrophages release mitochondria into MEVs, and under inflammatory conditions, package more damaged mitochondria into these vesicles.

MEVs from inflammatory macrophages exacerbate bone loss in periodontitis

To investigate the effects of MEVs from macrophages on periodontitis, we established an experimental periodontitis model in mice and intravenously injected Con-MEVs, *P.g*-MEVs, or PBS every 4 days (Fig. 2A) [29]. Four weeks after surgery, Micro-CT analysis revealed that the average CEJ-ABC distance was greater and that the bone volume fraction was lower in the *P.g*-MEV-treated group than in the other groups, suggesting a strong activation of bone loss by *P.g*-MEVs (Fig. 2B–D). The histological analysis revealed a similar trend (Fig. 2E–H). RUNX2 expression in the alveolar bone of mice treated with *P.g*-MEVs was significantly lower than that in the other groups, indicating that *P.g*-MEVs inhibit osteogenic activity (Fig. S4A).

We then administered MitoTracker-labeled macrophage-MEVs to the mice to examine the whole-body distribution of the transferred mitochondria of MEVs via in vivo imaging. The results revealed that approximately 60% of the fluorescence signals were in the liver, with higher concentrations also found in the kidneys and maxillae (Fig. 2I, Fig. S4B). The proportion of the fluorescence signals in the maxillae at 24 h was greater than that at 4 h. As shown in Fig. S4B, we separated only the maxilla, not the mandible, for fluorescence detection; therefore, the total fluorescence proportion in the entire alveolar bone should be greater. Furthermore, immunofluorescence staining revealed that the transferred mitochondria of macrophage-MEVs colocalized with a specific marker for

(See figure on next page.)

Fig. 2 MEVs from inflammatory macrophages transfer mitochondria to BMSCs, exacerbating alveolar bone loss in periodontitis. **A** Schematic diagram showing the experimental design. The untreated mice served as baseline controls. Periodontitis was induced by ligation combined with *P.g* coating for 28 days, and PBS, Con-MEVs, or *P.g*-MEVs were simultaneously injected via the tail vein. **B**–**H** Bone resorption was assayed and quantified by the distance from the cementoenamel junction (CEJ) to the alveolar bone crest (ABC) via Micro-CT (*vertical orange lines*) (**B**, **C**), hematoxylin and eosin (H&E) staining (*vertical yellow lines*) (**E**, **F**), and Masson's trichrome staining of the maxilla (*vertical yellow lines*) (**G**, **H**). The bone volume fraction was analyzed via Micro-CT (**D**). **I**, **J** To detect mitochondrial transfer in vivo, Con-MEVs and *P.g*-MEVs were labeled with MitoTracker (*red*) and then injected into mice, with PBS used as a control. **I** The average percentage of fluorescence distributed in the heart, liver, spleen, lungs, and kidneys was detected via IVIS Spectrum at 4 and 24 h postinjection. **J** Cryosections of the maxilla were subjected to immunofluorescence (IF) staining for SCA1 (green) and DAPI (blue), and images were obtained via confocal microscopy. Values were mean ± SD, n = 4 or 6. $^{*}P \le 0.05$, $^{***}P \le 0.001$, $^{****}P \le 0.0001$

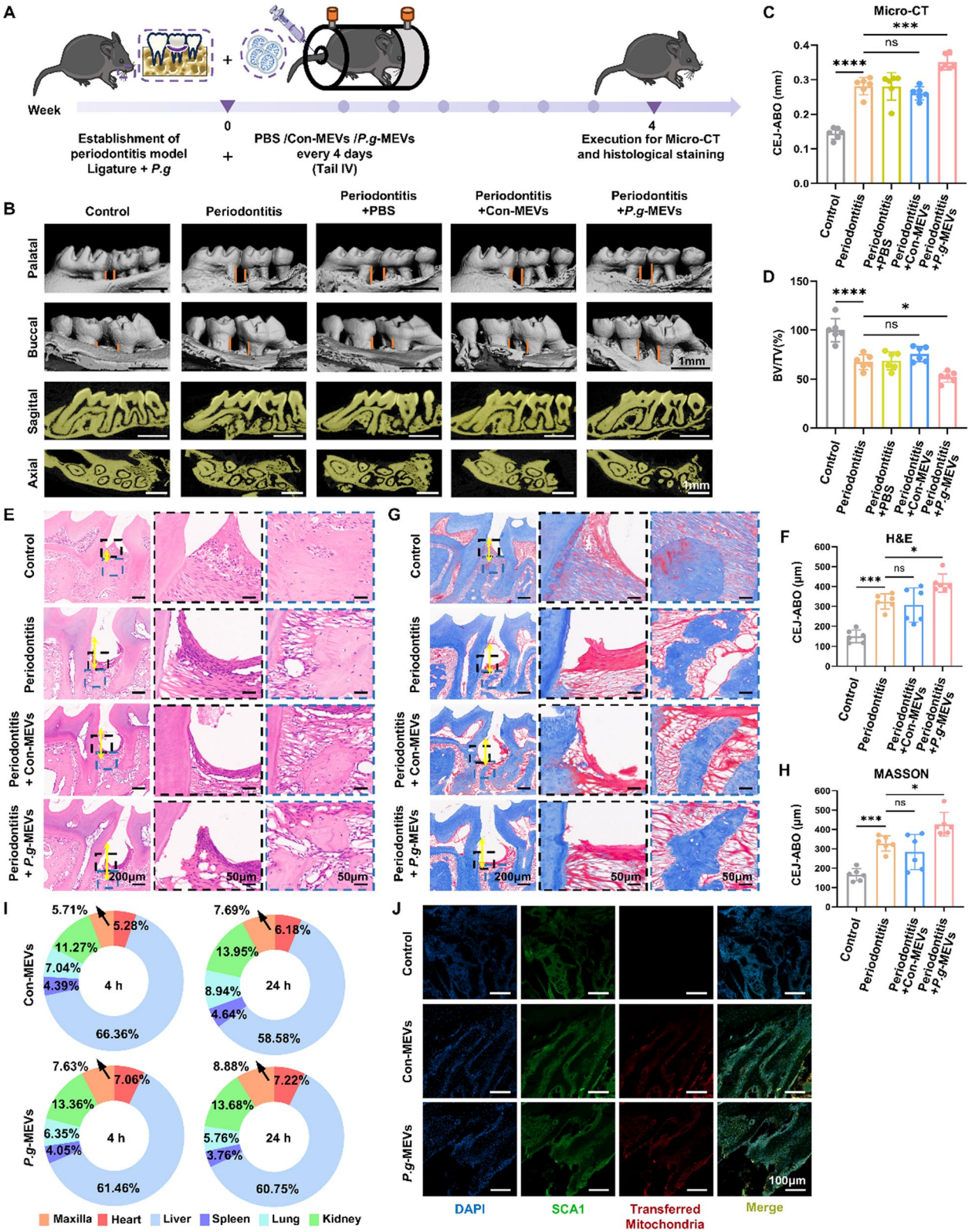

Fig. 2 (See legend on previous page.)

mesenchymal stem cells in the maxillae (Fig. 2J, Fig. S4C and D). Collectively, these results indicate that inflammatory macrophages exacerbate bone loss in periodontitis by transferring mitochondria to BMSCs via MEVs in the alveolar bone.

Transferred mitochondria from *P.g*-MEVs impede the osteogenic differentiation of BMSCs

These findings prompted us to assess the role of MEVs in the osteogenesis of BMSCs. MitoTracker was used to pre-label the mitochondria of macrophages (green) and BMSCs (red), and then, the macrophage-derived MEVs were cocultured with the BMSCs for 24 h. Confocal microscopy confirmed the presence of macrophage mitochondria within the BMSCs, and treatment with *P.g*-MEVs resulted in fragmented mitochondria in the BMSCs, with a reduction in filamentous mitochondria and an increase in punctate mitochondria (Fig. 3A). Analysis of the expression patterns of key osteogenic markers in BMSCs after osteogenic induction revealed that the expression of *Alp* (alkaline phosphatase) and *Runx2* (RUNX family transcription factor 2) was significantly lower in the *P.g*-MEVs group than in the other groups (Fig. 3B). Moreover, the osteogenic potential was confirmed by ARS staining, which revealed dramatic inhibition of matrix mineralization in BMSCs treated with *P.g*-MEVs (Fig. 3C, D).

An important question at this point is whether vesicles containing mitochondria within MEVs play a role in osteogenic inhibition or whether vesicles without mitochondria are effective. To address this question, we asked whether removing granules containing mitochondria from MEVs could reverse the osteogenic suppression of *P.g*-MEVs. As shown in Fig. 1C, the vesicles with mitochondria had a diameter larger than 220 nm. Therefore, we filtered the Con-MEVs and *P.g*-MEVs through a 220 nm filter, resulting in Con-MEVs-Large-particle-deleted (Con-MEVs-Ld) and *P.g*-MEVs-Ld. The NTA analysis indicated that filtration fundamentally removed particles larger than 220 nm from the MEVs (Fig. 3E). The flow cytometry results subsequently confirmed that removing particles larger than 220 nm effectively eliminated granules containing mitochondria in MEVs (Fig. 3F). ARS staining revealed that osteogenic ability was not significantly inhibited in the BMSCs incubated with *P.g*-MEVs-Ld, suggesting that the osteogenic inhibitory effect of *P.g*-MEVs was due to vesicles containing mitochondria (Fig. 3G, H).

Taken together, these results suggest that macrophages transfer mitochondria to BMSCs in an MEV-dependent manner and that the mitochondria from these two cell types are well integrated. The transfer of mitochondria from inflammatory macrophages to BMSCs via MEVs significantly suppressed the osteogenic differentiation of BMSCs.

The mitochondria of *P.g*-MEVs impede the formation of mitochondrial donuts in BMSCs

Considering the pivotal role of mitochondria in osteogenesis, which relies on changes in mitochondrial morphology, we subsequently explored whether the mechanism by which macrophages transfer mitochondria to BMSCs via MEVs and thereby inhibit osteogenesis is associated with disruptions in the mitochondrial dynamics of recipient cells. Fluorescence microscopy revealed that the formation of mitochondrial donuts was substantially augmented in BMSCs after osteogenic induction, peaking on day 7. In contrast, treatment of BMSCs with *P.g*-MEVs dramatically inhibited the formation of donut-shaped mitochondria (Fig. 4A, B). Similar results were obtained via TEM analysis (Fig. 4C). A decrease in ATP production is significantly correlated with the formation of mitochondrial donuts [30]. We also detected that the ATP levels in the BMSCs osteogenically induced for 3 days were greater than 5 μM, whereas those induced for 7 days were lower than 5 μM (Fig. 4D). However, the ATP concentrations in the BMSCs treated with *P.g*-MEVs were not significantly different from the other groups (Fig. 4D).

To identify the mechanisms involved in the regulation of mitochondrial donut formation, proteomic analysis was conducted on Con-MEVs and *P.g*-MEVs. A total of 528 DEPs were identified, with 130 downregulated and 398 upregulated, and the DEPs were mainly localized in the nucleus, the extracellular space, the plasma membrane, the cytoplasm, and the mitochondria (Fig. S5A and B). DEPs were subjected to GO, KEGG, and KOG annotation and enrichment. Most of the top 20 enriched terms were related to mitochondria and the formation and transport of vesicles (Fig. 4E–G). Numerous downregulated DEPs enriched in the glycolysis/gluconeogenesis and citrate cycle signaling pathways reflected damaged mitochondria in *P.g*-MEVs (Fig. S5C and D). Conserved GTPases in the dynamin family are required for mitochondrial dynamics, and both GTPase activity and GTP binding were identified as important differences (Fig. 4F). These findings indicate that the inhibition of mitochondrial donut formation and osteogenesis, which is mediated by the mitochondrial transfer of MEVs would be related to the disturbance of GTPase activity.

LCN2 plays a key role in controlling mitochondrial dynamics and osteogenesis by regulating OMA1 and OPA1

Previous studies have shown that LCN2 regulates mitochondrial dynamics [31]. In this study, we found that LCN2 in *P.g*-MEVs was upregulated by 8.7-fold compared

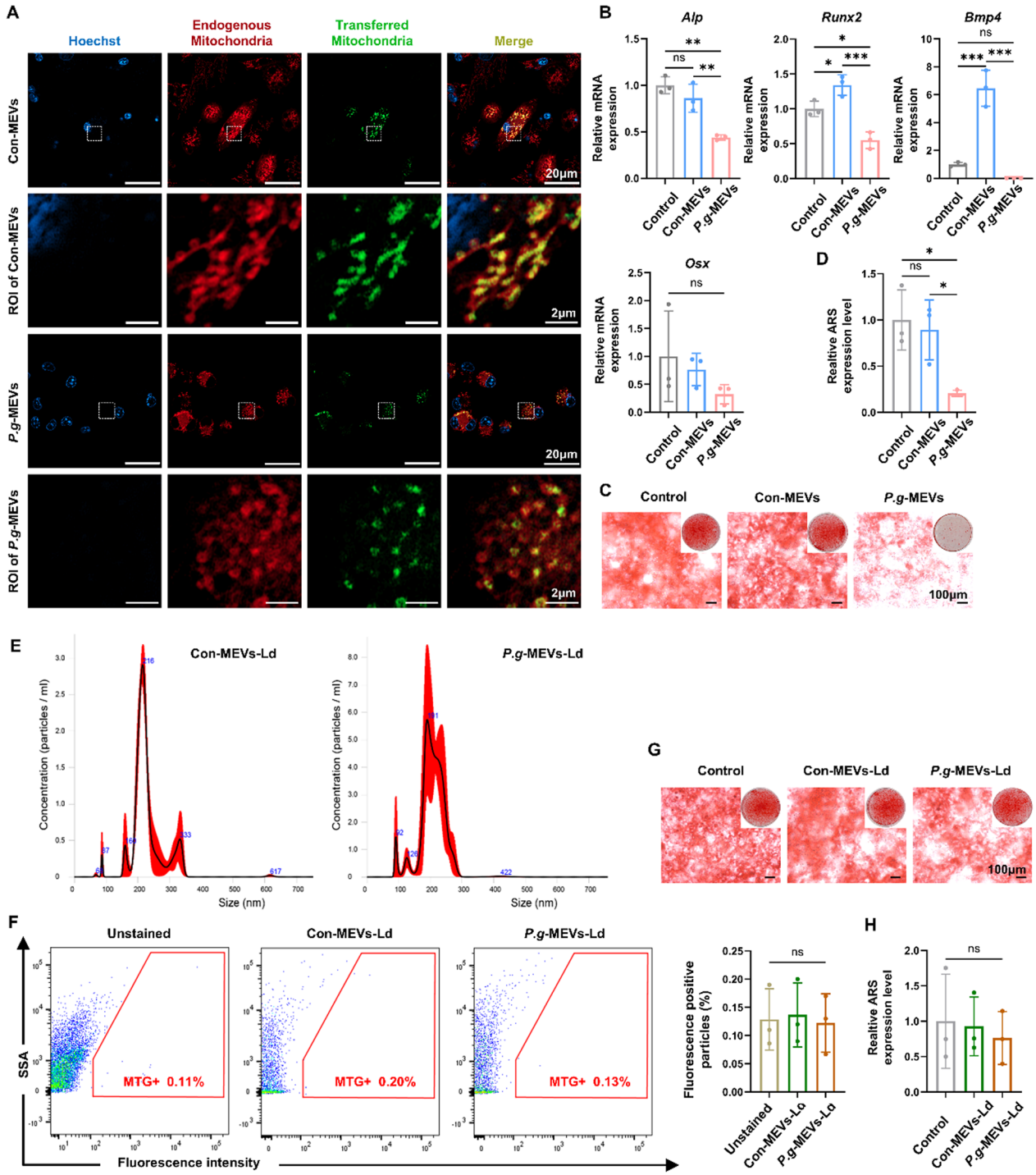

Fig. 3 MEVs from inflammatory macrophages significantly inhibit osteogenesis in BMSCs through the transfer of mitochondria. **A** Images of mitochondria transfer in vitro detected by a Zeiss LSM980 Airyscan confocal microscope. Con-MEVs and *P.g*-MEVs were extracted from macrophages labeled with MitoTracker (*green*). The BMSCs were preliminarily stained with MitoTracker (*red*) and Hoechst and then cocultured with MEVs for 24 h. **B** The mRNA expression levels of *Alp*, *Runx2*, *Bmp4* and *Osx* were detected via qRT-PCR, with *β-actin* as an internal control, in BMSCs after osteogenic induction for 7 days. **C**, **D** Mineralized nodules were detected by Alizarin Red S (ARS) staining in BMSCs after osteogenic induction for 21 days. Semiquantitative analysis was performed via solubilization with cetylpyridinium chloride. **E**–**H** To remove mitochondria-containing vesicles, Con-MEVs and *P.g*-MEVs were subjected to a 0.22 μm filter, resulting in Con-MEVs-Large-particle-deleted (Con-MEVs-Ld) and *P.g*-MEVs-Ld. **E** Particle size distribution was detected via NTA. **F** The frequency of mitochondria was tested by flow cytometry. **G**, **H** Mineralized nodules were detected via ARS staining, and semiquantitative analyses were performed. BMSCs were osteogenically induced for 21 days with or without MEVs-Ld. Values were mean ± SD, n = 3. *$P \le 0.05$, **$P \le 0.01$, ***$P \le 0.001$

with that in Con-MEVs (Fig. 5A). Western blot analysis revealed that LCN2 in macrophages and MEVs was significantly upregulated under periodontitis conditions and that LCN2 colocalized with the mitochondria in macrophages (Fig. 5B, Fig. S6A). Consistent with the results of the cell-based experiments, immunohistochemical staining revealed that LCN2 expression in alveolar bone was significantly greater in the mice with periodontitis than in the controls (Fig. S6B).

It has been suggested that the downregulation of OPA1 promotes the formation of mitochondrial donuts during osteogenesis. We also detected that the expressions of LCN2 and OPA1 was both significantly downregulated in the BMSCs after 7 days of osteogenic induction, indicating that LCN2 may play a role in regulating OPA1 and donut-shaped mitochondria (Fig. 5C). In contrast, *P.g*-MEVs induced significant upregulation of LCN2 in BMSCs and LCN2 colocalized with mitochondria (Fig. S6C and D). The degradation of OPA1 by OMA1 triggers adaptive morphological changes in mitochondria in response to stress. We further found that upregulation of LCN2 inhibited OMA1 in BMSCs incubated with *P.g*-MEVs.

Finally, we constructed LCN2-overexpressing BMSCs via lentivirus and found that LCN2 overexpression significantly downregulated OMA1 and upregulated OPA1 (Fig. 5D). Moreover, the upregulation of LCN2 dramatically impaired mitochondrial donut formation and osteogenesis (Fig. 5E–G). However, we found that the LCN2 inhibitor (10 μM/mL, ZINC00640089) rescued BMSCs from the inhibitory effects of *P.g*-MEVs on the formation of mitochondrial donuts and osteogenesis (Fig. 5H, I). The administration of the LCN2 inhibitor to mice via the tail vein (10 μM/mL, 100 μL) significantly reversed alveolar bone loss in periodontitis (Fig. 5J).

These results revealed that LCN2 was upregulated in MEVs derived from inflammatory macrophages. The entry of LCN2, along with transferred mitochondria, into BMSCs led to the dysregulation of OMA1 and OPA1, thereby affecting the mitochondrial dynamics and osteogenesis of BMSCs and resulting in alveolar bone resorption. Inhibition of LCN2 rescued bone loss in periodontitis.

Discussion

BMSCs, the primary source of osteoblasts, play broad roles in maintaining homeostasis and repairing of alveolar bone [4]. There has been interest in rescuing BMSCs to promote clinical bone regeneration in periodontitis [5]. These efforts have been complicated by limited understanding of the mechanisms involved in the osteogenic impairment of BMSCs. MEVs regulate both healthy and pathological states in many organ systems, but the mechanisms of their biogenesis, ability to dock to target cells, ability to be internalized, and functional roles within recipient cells are poorly understood, especially in periodontitis [32, 33]. In this study, we revealed that MEVs mediated mitochondrial transfer between macrophages and BMSCs, and played a pivotal role in osteogenic inhibition of BMSCs in periodontitis. We also demonstrated novel regulatory mechanisms of MEVs in BMSCs by altering mitochondrial dynamics, and we partially elucidated the molecular mechanisms underlying this regulatory effect.

MEVs are medium to large EVs that encapsulate mitochondria, with diameters ranging from 100 to 1000 nm, and are produced by direct budding and shedding from the plasma membrane [34]. Consistent with this, we found that the diameters of both Con-MEVs and *P.g*-MEVs ranged from 100 to 600 nm. The cargo encapsulated by EVs originates from the parent cell and is regulated by the physiological state and stress conditions of the parent cell. For example, hypoxia leads to an increase in hypoxia-related proteins in EVs derived from glioma cells [35]. Similarly, the mitochondria in MEVs also synchronize with those in parent cells. Compared with those cultured for 50 days, induced pluripotent stem cell-derived cardiomyocytes released more functional mitochondria to MEVs when cultured for 15 days [36]. We also found that *P.g*-MEVs contained more damaged mitochondria, which is consistent with the obvious mitochondrial dysfunction in macrophages after infection with *P.g*.

Some cell types export their mitochondria and transport them to developmentally unrelated cell types, and this process is called intercellular mitochondria transfer [19]. Four distinct modes of intercellular mitochondria

(See figure on next page.)

Fig. 4 Inflammatory macrophage-derived MEVs disrupted mitochondrial dynamics and hindered mitochondrial donut formation in BMSCs. **A**, **B** Mitochondrial morphology in BMSCs cocultured with or without MEVs during osteogenic induction was visualized via confocal microscopy. The *white arrows* indicate mitochondrial donuts. The percentage of donut-shaped mitochondria was quantified at days 3 and 7. **C** Representative TEM images of mitochondria in BMSCs after osteogenic induction for 7 days. **D** ATP content in BMSCs cocultured with or without MEVs during osteogenic induction was measured. **E**–**G** Bubble charts showing the top 20 significantly enriched terms in the KEGG, GO, and KOG analyses of differentially expressed proteins (DEPs) in Con-MEVs and *P.g*-MEVs, as revealed by proteomic analysis and enrichment analysis. Values were mean ± SD, n = 3 or 6. $^{**}P \leq 0.01$

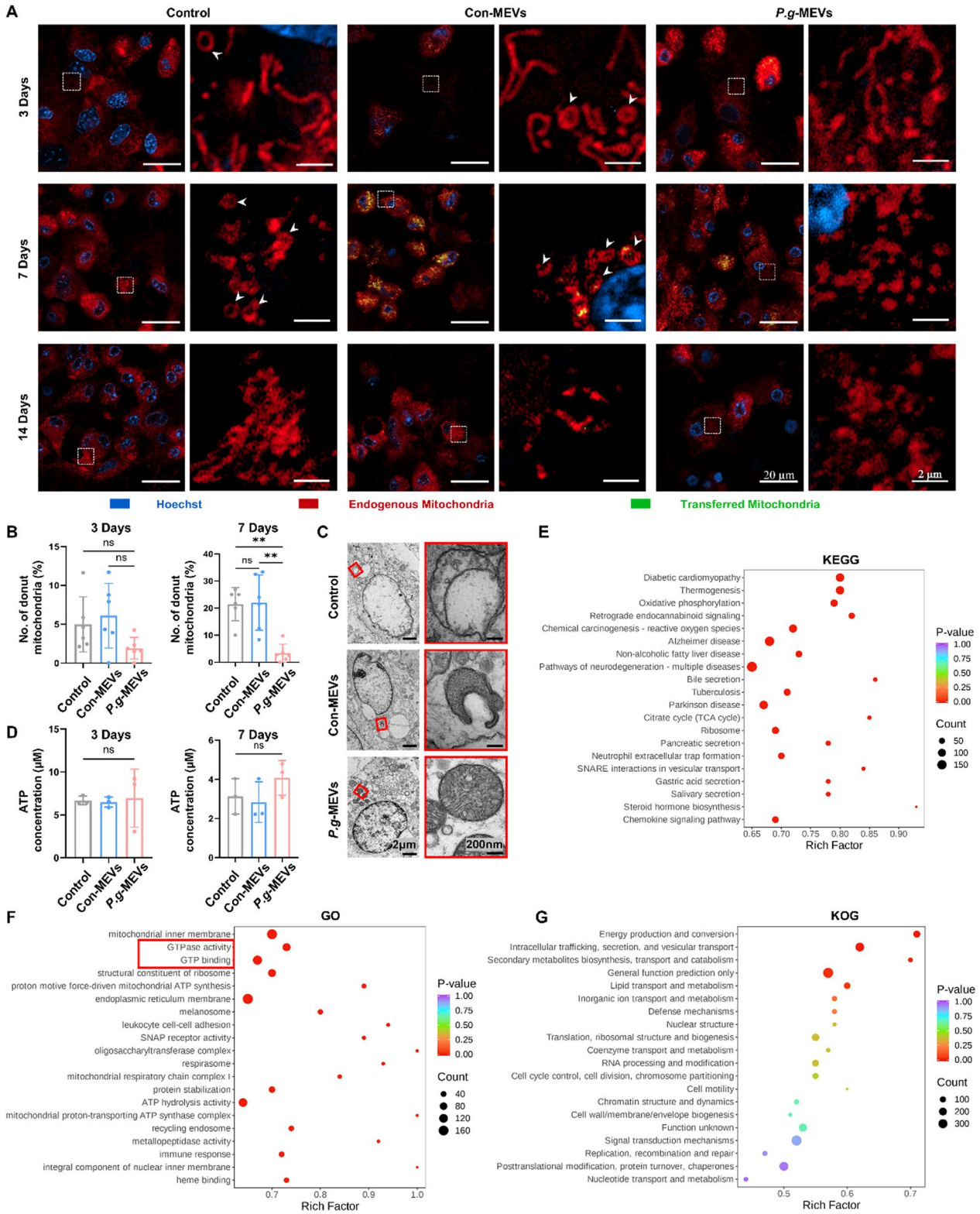

Fig. 4 (See legend on previous page.)

transfer have been reported in the literature [19]. Given that most macrophages are distributed in the gingiva and that MSCs are located in the alveolar bone, it is reasonable to speculate that mitochondrial crosstalk between macrophages and MSCs is likely to occur through MEVs. This method operates in an extracellular vesicle-dependent manner, wherein donor cells release MEVs for delivery to recipient cells, with the importance of protecting and facilitating long-distance transfer of mitochondria via lipid membrane encapsulation [22]. We found that the mitochondria of inflammatory macrophages were significantly damaged and subsequently secreted into MEVs, which accumulated in the maxilla over time and exacerbated bone loss in periodontitis.

Most reports suggest that MEVs containing undamaged mitochondria support the functions of recipient cells [19]. For example, astrocytes deliver MEVs and support neuron survival after stroke through a CD38/cADPR-dependent process, and macrophages transport MEVs to neurons via a process mediated by CD200R-iSec1 to suppress inflammatory pain [21, 37]. While current research on EVs containing damaged mitochondria has focused mainly on those associated with the Pink1-Parkin pathway, these vesicles are 100–200 nm in size [19, 22]. Oxidative stress prompts adipocytes to package damaged mitochondria into EVs in a Parkin-dependent manner, which are then delivered to cardiomyocytes for integration into their mitochondrial network [22]. Moreover, damaged mitochondria within adipocyte-derived EVs are degraded by lysosomes after their internalization by macrophages [19]. Therefore, we speculate that the fate of mitochondria in MEVs after internalization by recipient cells may be related to downstream factors of this process, such as target cell types or processing pathways, rather than to the mechanisms of MEV formation and release. The macrophage MEVs in our study were mostly larger than 200 nm, and the mechanism of *P.g*-MEV formation should be independent of Pink1-Park. After *P.g*-MEVs are internalized by BMSCs, further investigation into how macrophagic mitochondria integrate into the BMSC mitochondrial network is warranted. This could enhance our understanding of the intracellular localization and functional regulation following MEV internalization by recipient cells.

Mitochondrial transfer has been reported to regulate the metabolism of recipient cells, for example, by promoting ATP generation to support the survival of neurons after ischemic stroke, leading to the reprogramming of oxidative phosphorylation in tumor cells [37, 38]. However, we found that macrophages transferred mitochondria via MEVs to BMSCs, where mitochondrial dynamics were disrupted instead of ATP production. There is a complex transition between oxidative phosphorylation and glycolytic metabolism during osteogenic differentiation. Although we found that *P.g*-MEVs did not significantly alter ATP levels in BMSCs at days 3 and 7 postosteogenic induction, the specific effects of *P.g*-MEVs on the levels of oxidative phosphorylation and glycolytic metabolism in BMSCs during osteogenic differentiation require further investigation. Consistent with the findings of a previous study, we reported that during osteogenesis, mitochondria underwent adaptive morphological changes from a filamentous shape to a donut-like shape [12]. The transferred mitochondria hindered donut-shaped mitochondria formation, severely impairing osteogenesis. Although we did not visualize the actual moment of mitochondria transfer in vivo, our data provide the most definitive evidence to date, suggesting that mitochondrial transfer via MEVs is an important mechanism of bone loss in periodontitis. BMSCs also secrete MEVs that load calcium phosphate mineralization particles for extracellular biomineralization, and the regulation of this complete biological process by macrophage mitochondria transfer still needs to be investigated.

Furthermore, we found significant enrichment in GTPase activity and GTP binding pathways via proteomic analysis of MEVs. These findings suggest that MEVs regulated mitochondrial dynamics in BMSCs via GTPases. The continuous morphological changes in mitochondria are controlled by a variety of GTPases, with OPA1 being

(See figure on next page.)

Fig. 5 LCN2 regulates OMA1 and OPA1, thereby disrupting the formation of mitochondrial donuts and osteogenesis. **A** Volcano plot showing significant DEPs (fold change > 1.5 or <0.6667 and *P*-value < 0.05), with the top 10 upregulated proteins annotated. **B** The expression of LCN2 in macrophages and MEVs was detected by Western blotting, with β-actin as the internal control. **C** The expression of OPA1 and LCN2 in BMSCs was detected by Western blotting at 0, 3, 7, and 14 days after osteogenic induction. **D**–**G** LCN2 was overexpressed in BMSCs via lentiviral transduction, and the empty vector was used as a negative control (NC). **D** The expression of LCN2, OMA1 and OPA1 was detected by Western blotting after 7 days of osteogenic induction. **E** The formation of mitochondrial donuts was detected by confocal microscopy. The *white arrows* indicate mitochondrial donuts. **F**, **G** ARS staining was used to detect the formation of mineralized nodules in BMSCs after 21 days of osteogenic induction. **H**–**J** An LCN2 inhibitor (ZINC00640089, 10 μM) was used to validate the therapeutic potential of LCN2 in periodontitis. **H** Representative images of mitochondrial morphology, and **I** ARS staining of osteogenically induced BMSCs cocultured with *P.g*-MEVs and LCN2 inhibitors. **J** Bone resorption was assayed by the distance from the CEJ to the ABC (*vertical orange lines*) and by the bone volume fraction as determined by Micro-CT. Values were mean ± SD, n = 3 or 6. *$P \le 0.05$, **$P \le 0.01$, ***$P \le 0.001$.

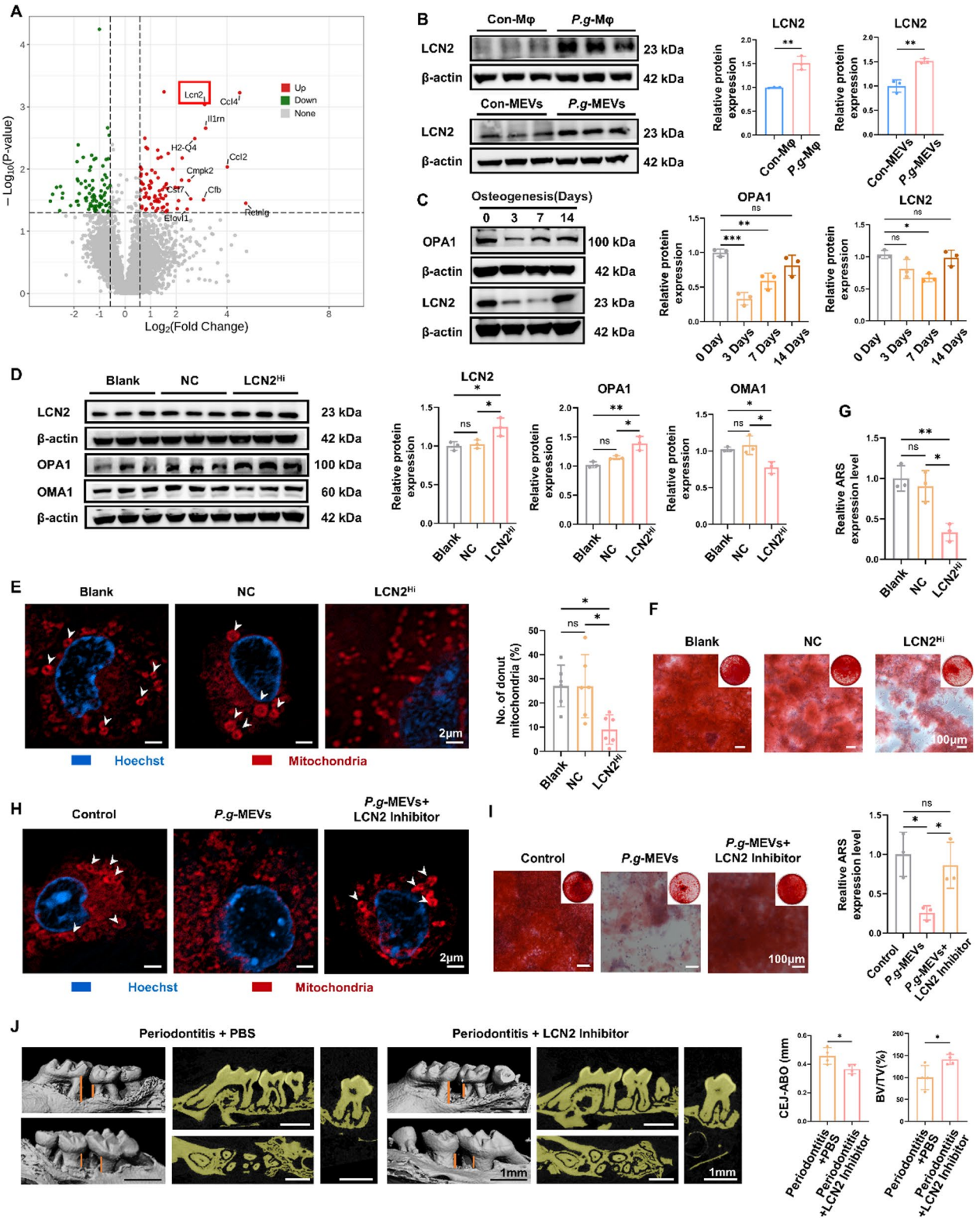

Fig. 5 (See legend on previous page.)

crucial [39]. OPA1 promotes the fusion of the mitochondrial inner membrane, and the proteolytic products separate the mitochondrial inner membrane from the outer membrane [39]. During osteogenesis, an increase in OPA1 proteolysis drives mitochondrial donut formation. OMA1 responds to mitochondrial stress, including decreased ATP levels, by cleaving OPA1 at the S1 site, which may play a role in osteogenesis [40, 41]. LCN2 is a key component of the innate immune response [42–44]. Recent evidence revealed the regulatory function of LCN2 in mitochondria [31, 45], but it remains unclear whether LCN2 acts on OPA1 and OMA1. We found that OMA1 was downregulated and that OPA1 was upregulated by LCN2 in periodontitis, perturbing mitochondrial morphological changes and resulting in the dysfunction of BMSCs. While mitochondrial dynamic regulation and organization are also driven by other proteins in the dynamin superfamily, such as DRP1 (dynamin-related protein 1), MFN1 and MFN2 (mitofusins 1 and 2), the specific regulatory role of these proteins on mitochondrial donut has not yet been revealed.

We found that the mitochondria did not exhibit excessive fusion but rather fragmentation when the OPA1 protein accumulated in the BMSCs. This may be due to the mitochondrial safeguard mechanism in the cells, where OPA1, which controls mitochondrial fusion, and DRP1, which controls mitochondrial fission, exhibit a coordinated protein expression trend [46]. We speculated that the accumulation of OPA1 in BMSCs simultaneously induced the upregulation of DRP1, leading to mitochondrial fragmentation, which requires further study. We preliminarily suggested that mitochondrial transfer altered the abundance of proteins with GTPase regulatory functions in BMSCs, which disturbed mitochondrial dynamics and osteogenesis. However, the impact of the signals carried by transferred mitochondria, including proteins, nucleic acids, and phospholipids, on recipient cells still requires further research.

Conclusions

Despite these limitations, we demonstrated that the MEVs of macrophages in periodontitis respond to inflammatory stimuli by regulating mitochondrial dynamics in BMSCs through mitochondrial transfer, which hinders the osteogenesis of BMSCs. Furthermore, this process increased LCN2 in BMSCs, resulting in the degradation of OMA1 and the accumulation of OPA1, leading to an imbalance in mitochondrial dynamics and impaired donut formation, thereby exacerbating bone loss in periodontitis. Inhibition of LCN2 rescued alveolar bone loss in periodontitis, suggesting a promising therapeutic strategy for periodontitis.

Abbreviations

Alp	Alkaline phosphatase
Bmp4	Bone morphogenetic protein 4
CD29, 63	Cluster of differentiation 29, 63
ECL	Enhanced chemiluminescence
EDTA	Ethylenediaminetetraacetic acid
FBS	Fetal bovine serum
H&E	Hematoxylin and eosin
Il-1β	Interleukin-1 beta
IL-6Il-6	Interleukin-6
LC–MS/MS	Liquid chromatography-tandem mass spectrometry
LCN2	Lipocalin2
MEVs	Mitochondria-rich extracellular vesicles
Micro-CT	Micro computed tomography
Mφ	Macrophages
MOI	Multiplicity of infection
MTDR	MitoTracker Deep Red
MTG	MitoTracker Green
Nos2	Nitric oxide synthase 2
OPA1	Optic atrophy 1
Osx	Osterix
P.g	*Porphyromonas gingivalis*
PBS	Phosphate-buffered saline
RT–qPCR	Real-time quantitative PCR
Runx2	Runt-related transcription factor 2
SDS	Sodium dodecyl sulfate
TEM	Transmitted electron microscopy
TNF-α	Tumor necrosis factor-α

Supplementary Information

The online version contains supplementary material available at https://doi.org/10.1186/s12951-025-03178-4.

Additional file 1: Fig. S1. Compared with uninfected macrophages, macrophages infected with *P.g* presented significantly increased inflammatory levels. (A) Primary macrophages were characterized via flow cytometry. (B) The mRNA expression levels of *IL-1β*, *TNF-α*, *IL-6*, and *Nos2* in macrophages were measured before and after infection with *P.g*, with *β-actin* as an internal control, via qRT-PCR. Values were mean±SD, n = 3. * $P \leq 0.05$, **** $P \leq 0.0001$. Fig. S2. The mitochondria of macrophages are damaged by *P.g* infection. (A) Representative images of mitochondria in macrophages under PBS and *P.g* infection conditions. (B) Mitochondrial membrane potential in macrophages was determined by JC-1. (C) Relative levels of mitochondrial reactive oxygen species (ROS) were detected by the mean fluorescence intensity ratio of MitoSOX to MitoTracker. Values were mean±SD, n = 3. * $P \leq 0.05$, ** $P \leq 0.01$. Fig. S3. The average diameters (A) and average concentrations (B) of MEVs derived from macrophages before and after infection were measured via nanoparticle tracking analysis. Values were mean±SD, n = 3-6. Fig. S4. MEVs from inflammatory macrophages transfer mitochondria to periodontal tissues, thereby inhibiting the osteogenic activity of alveolar bone. (A) Immunohistochemistry (IHC) staining for RUNX2 in the maxillae of mice. The percentage of RUNX2-positive areas in alveolar bone was measured. (B) Images of the tissue distribution of fluorescence signals in mice after treatment with MitroTracker-labeled MEVs. (C, D) Cryosections of the gingiva and periodontal ligament were subjected to immunofluorescence (IF) staining for SCA1(green) and DAPI (blue), and images were obtained via confocal microscopy. The white line delineates the boundary between the crown (c), gingiva (g), root (r), periodontal ligament (p), and alveolar bone (a). Values were mean±SD, n=3. * $P \leq 0.05$, *** $P \leq 0.001$. Fig. S5. Proteomic analysis of differentially expressed proteins (DEPs) in Con-MEVs and *P.g*-MEVs. (A) Heatmap showing a total of 528 DEPs, with 130 downregulated and 398 upregulated. (B) Subcellular structure location analysis revealed that the DEPs were mainly localized in the nucleus, extracellular space, plasma membrane, cytoplasm, and mitochondria. (C, D) DEPs enriched in the glycolysis/gluconeogenesis and citrate cycle signaling pathways. Fig. S6. LCN2 expression was upregulated in periodontitis. (A) IF staining of LCN2 (red) and mitochondria (green) in macrophages before and after infection. Uninfected macrophages served as a control (Con-Mφ),

while macrophages infected with *P.g* were designated *P.g*-Mφ. (B) IHC staining for LCN2 in the maxillae of mice with or without periodontitis. The percentage of LCN2-positive areas in alveolar bone was measured. (C, D) BMSCs were cultured in osteogenic induction medium, with or without the addition of MEVs. (C) BMSCs were subjected to IF staining for LCN2 (red) and mitochondria (green). (D) The expression of LCN2, OMA1 and OPA1 was detected by Western blotting, with β-actin as the internal control. Values were mean±SD, n = 3. * $P \leq 0.05$, ** $P \leq 0.01$, *** $P \leq 0.001$, **** $P \leq 0.0001$.

Additional file 2: Table S1. Primer sequences.

Acknowledgements
We thank Huiming Zheng and Tong Yan for their editorial assistance.

Funding
This study was supported by the National Natural Science Foundation of China (no.82471013,82270985) and the Guangzhou Key Research and Development Program (no.2024B03J0497).

Declarations

Ethics approval and consent to participate
Male C57BL/6 mice (4–12 weeks) were purchased from Sun Yat-sen University Laboratory Animal Center. All experiments were performed following guidelines approved by the Animal Ethics Committee of Sun Yat-Sen University (SYSU-IACUC-2022-002192), Guangzhou, China, and conformed to the ARRIVE Guidelines.

Consent for publication
All the authors have approved the manuscript and agree with its publication.

Competing interests
The authors declare no competing interests.

Author contributions
JY contributed to the conception and design, acquisition, analysis, and interpretation of data, drafted manuscript, and critically revised manuscript; TY contributed to the acquisition of data, and drafted manuscript; SM contributed to the acquisition and analysis of data, and critically revised manuscript; DL contributed to the acquisition and interpretation of data, and critically revised manuscript; CH contributed to the design, and critically revised manuscript; JT contributed to the funding acquisition, and supervision. All the authors gave final approval and agreed to be accountable for all aspects of the work.

Availability of data and materials
The relevant experimental data are available from the corresponding author upon reasonable request.

Author details
[1]Hospital of Stomatology, Sun Yat-sen University, Guangzhou 510055, China. [2]Guangdong Provincial Key Laboratory of Stomatology, Sun Yat-sen University, Guangzhou 510080, China. [3]Guanghua School of Stomatology, Sun Yat-sen University, Guangzhou 510080, China. [4]Institute of Stomatology, Sun Yat-sen University, Guangzhou 510080, China.

Received: 18 November 2024 Accepted: 31 January 2025
Published online: 12 March 2025

References

1. Hajishengallis G. Interconnection of periodontal disease and comorbidities: Evidence, mechanisms, and implications. Periodontol 2000. 2022;89(1):9–18.
2. Hajishengallis G, Chavakis T. Local and systemic mechanisms linking periodontal disease and inflammatory comorbidities. Nat Rev Immunol. 2021;21(7):426–40.
3. Kwon T, Lamster IB, Levin L. Current concepts in the management of periodontitis. Int Dent J. 2021;71(6):462–76.
4. Li P, Ou Q, Shi S, Shao C. Immunomodulatory properties of mesenchymal stem cells/dental stem cells and their therapeutic applications. Cell Mol Immunol. 2023;20(6):558–69.
5. Chen Y, Wang H, Yang Q, Zhao W, Chen Y, Ni Q, et al. Single-cell RNA landscape of the osteoimmunology microenvironment in periodontitis. Theranostics. 2022;12(3):1074–96.
6. Wang H, Chang X, Ma Q, Sun B, Li H, Zhou J, et al. Bioinspired drug-delivery system emulating the natural bone healing cascade for diabetic periodontal bone regeneration. Bioact Mater. 2023;21:324–39.
7. Govindaraj P, Khan NA, Gopalakrishna P, Chandra RV, Vanniarajan A, Reddy AA, et al. Mitochondrial dysfunction and genetic heterogeneity in chronic periodontitis. Mitochondrion. 2011;11(3):504–12.
8. Yang H, Zhao A, Chen Y, Cheng T, Zhou J, Li Z. Exploring the potential link between MitoEVs and the immune microenvironment of periodontitis based on machine learning and bioinformatics methods. BMC Oral Health. 2024;24(1):169.
9. Deng Y, Xiao J, Ma L, Wang C, Wang X, Huang X, et al. Mitochondrial dysfunction in periodontitis and associated systemic diseases: implications for pathomechanisms and therapeutic strategies. Int J Mol Sci. 2024;25(2):1024.
10. Iwayama T, Okada T, Ueda T, Tomita K, Matsumoto S, Takedachi M, et al. Osteoblastic lysosome plays a central role in mineralization. Sci Adv. 2019;5(7):eaax0672.
11. Tang C, Wei Y, Gu L, Zhang Q, Li M, Yuan G, et al. Biomineral precursor formation is initiated by transporting calcium and phosphorus clusters from the endoplasmic reticulum to mitochondria. Adv Sci (Weinh). 2020;7(8):1902536.
12. Suh J, Kim NK, Shim W, Lee SH, Kim HJ, Moon E, et al. Mitochondrial fragmentation and donut formation enhance mitochondrial secretion to promote osteogenesis. Cell Metab. 2023;35(2):345-60.e7.
13. Parisi L, Gini E, Baci D, Tremolati M, Fanuli M, Bassani B, et al. Macrophage polarization in chronic inflammatory diseases: killers or builders? J Immunol Res. 2018;2018:8917804.
14. Pajarinen J, Lin T, Gibon E, Kohno Y, Maruyama M, Nathan K, et al. Mesenchymal stem cell-macrophage crosstalk and bone healing. Biomaterials. 2019;196:80–9.
15. Boyce BF. Advances in the regulation of osteoclasts and osteoclast functions. J Dent Res. 2013;92(10):860–7.
16. Xiao J, Deng Y, Xie J, Liu H, Yang Q, Zhang Y, et al. Apoptotic vesicles from macrophages exacerbate periodontal bone resorption in periodontitis via delivering miR-143-3p targeting Igfbp5. J Nanobiotechnology. 2024;22(1):658.
17. Valadi H, Ekström K, Bossios A, Sjöstrand M, Lee JJ, Lötvall JO. Exosome-mediated transfer of mRNAs and microRNAs is a novel mechanism of genetic exchange between cells. Nat Cell Biol. 2007;9(6):654–9.
18. Kwak G, Cheng J, Kim H, Song S, Lee SJ, Yang Y, et al. Sustained exosome-guided macrophage polarization using hydrolytically degradable PEG hydrogels for cutaneous wound healing: identification of key proteins and MiRNAs, and sustained release formulation. Small. 2022;18(15): e2200060.
19. Borcherding N, Brestoff JR. The power and potential of mitochondria transfer. Nature. 2023;623(7986):283–91.
20. Puhm F, Afonyushkin T, Resch U, Obermayer G, Rohde M, Penz T, et al. Mitochondria are a subset of extracellular vesicles released by activated monocytes and induce type I IFN and TNF responses in endothelial cells. Circ Res. 2019;125(1):43–52.
21. Vlist M, Raoof R, Willemen H, Prado J, Versteeg S, Martin Gil C, et al. Macrophages transfer mitochondria to sensory neurons to resolve inflammatory pain. Neuron. 2022;110(4):613-26.e9.
22. Crewe C, Funcke JB, Li S, Joffin N, Gliniak CM, Ghaben AL, et al. Extracellular vesicle-based interorgan transport of mitochondria from energetically stressed adipocytes. Cell Metab. 2021;33(9):1853-68.e11.
23. Zhao X, Liu J, Zhang C, Yu N, Lu Z, Zhang S, et al. *Porphyromonas gingivalis* exacerbates ulcerative colitis via *Porphyromonas gingivalis* peptidylarginine deiminase. Int J Oral Sci. 2021;13(1):31.
24. Angabo S, Pandi K, David K, Steinmetz O, Makkawi H, Farhat M, et al. CD47 and thrombospondin-1 contribute to immune evasion by *Porphyromonas gingivalis*. Proc Natl Acad Sci U S A. 2024;121(47): e2405534121.

25. Tanai A, Fukuhara Y, Eguchi T, Kawai H, Ueda K, Ochiai K, et al. *P. gingivalis*-infected macrophage extracellular vesicles cause adverse pregnancy outcomes. J Dent Res. 2024;104(1):54–63.
26. Ikeda G, Santoso MR, Tada Y, Li AM, Vaskova E, Jung JH, et al. Mitochondria-rich extracellular vesicles from autologous stem cell-derived cardiomyocytes restore energetics of ischemic myocardium. J Am Coll Cardiol. 2021;77(8):1073–88.
27. Falchi AM, Sogos V, Saba F, Piras M, Congiu T, Piludu M. Astrocytes shed large membrane vesicles that contain mitochondria, lipid droplets and ATP. Histochem Cell Biol. 2013;139(2):221–31.
28. Arifin WN, Zahiruddin WM. Sample size calculation in animal studies using resource equation approach. Malays J Med Sci. 2017;24(5):101–5.
29. Mu S, Tee BC, Emam H, Zhou Y, Sun Z. Culture-expanded mesenchymal stem cell sheets enhance extraction-site alveolar bone growth: an animal study. J Periodontal Res. 2018;53(4):514–24.
30. Liu X, Hajnóczky G. Altered fusion dynamics underlie unique morphological changes in mitochondria during hypoxia-reoxygenation stress. Cell Death Differ. 2011;18(10):1561–72.
31. Marques E, Alves Teixeira M, Nguyen C, Terzi F, Gallazzini M. Lipocalin-2 induces mitochondrial dysfunction in renal tubular cells via mTOR pathway activation. Cell Rep. 2023;42(9): 113032.
32. Watson DC, Bayik D, Storevik S, Moreino SS, Sprowls SA, Han J, et al. GAP43-dependent mitochondria transfer from astrocytes enhances glioblastoma tumorigenicity. Nat Cancer. 2023;4(5):648–64.
33. Rosina M, Ceci V, Turchi R, Chuan L, Borcherding N, Sciarretta F, et al. Ejection of damaged mitochondria and their removal by macrophages ensure efficient thermogenesis in brown adipose tissue. Cell Metab. 2022;34(4):533-48.e12.
34. D'Souza A, Burch A, Dave KM, Sreeram A, Reynolds MJ, Dobbins DX, et al. Microvesicles transfer mitochondria and increase mitochondrial function in brain endothelial cells. J Control Release. 2021;338:505–26.
35. Kucharzewska P, Christianson HC, Welch JE, Svensson KJ, Fredlund E, Ringnér M, et al. Exosomes reflect the hypoxic status of glioma cells and mediate hypoxia-dependent activation of vascular cells during tumor development. Proc Natl Acad Sci U S A. 2013;110(18):7312–7.
36. Malekpour K, Hazrati A, Soudi S, Hashemi SM. Mechanisms behind therapeutic potentials of mesenchymal stem cell mitochondria transfer/delivery. J Control Release. 2023;354:755–69.
37. Hayakawa K, Esposito E, Wang X, Terasaki Y, Liu Y, Xing C, et al. Transfer of mitochondria from astrocytes to neurons after stroke. Nature. 2016;535(7613):551–5.
38. Del Vecchio V, Rehman A, Panda SK, Torsiello M, Marigliano M, Nicoletti MM, et al. Mitochondrial transfer from Adipose stem cells to breast cancer cells drives multi-drug resistance. J Exp Clin Cancer Res. 2024;43(1):166.
39. Nyenhuis SB, Wu X, Strub MP, Yim YI, Stanton AE, Baena V, et al. OPA1 helical structures give perspective to mitochondrial dysfunction. Nature. 2023;620(7976):1109–16.
40. Xiao X, Hu Y, Quirós PM, Wei Q, López-Otín C, Dong Z. OMA1 mediates OPA1 proteolysis and mitochondrial fragmentation in experimental models of ischemic kidney injury. Am J Physiol Renal Physiol. 2014;306(11):F1318–26.
41. Murata D, Roy S, Lutsenko S, Iijima M, Sesaki H. Slc25a3-dependent copper transport controls flickering-induced Opa1 processing for mitochondrial safeguard. Dev Cell. 2024;59(19):2578-2592.e7.
42. Gupta U, Ghosh S, Wallace CT, Shang P, Xin Y, Nair AP, et al. Increased LCN2 (lipocalin 2) in the RPE decreases autophagy and activates inflammasome-ferroptosis processes in a mouse model of dry AMD. Autophagy. 2023;19(1):92–111.
43. Xiao X, Yeoh BS, Vijay-Kumar M. Lipocalin 2: an emerging player in iron homeostasis and inflammation. Annu Rev Nutr. 2017;37:103–30.
44. Paudel D, Nair DVT, Tian S, Hao F, Goand UK, Joseph G, et al. Dietary fiber guar gum-induced shift in gut microbiota metabolism and intestinal immune activity enhances susceptibility to colonic inflammation. Gut Microbes. 2024;16(1):2341457.
45. Su H, Guo H, Qiu X, Lin TY, Qin C, Celio G, et al. Lipocalin 2 regulates mitochondrial phospholipidome remodeling, dynamics, and function in brown adipose tissue in male mice. Nat Commun. 2023;14(1):6729.
46. Murata D, Yamada T, Tokuyama T, Arai K, Quirós PM, López-Otín C, et al. Mitochondrial Safeguard: a stress response that offsets extreme fusion and protects respiratory function via flickering-induced Oma1 activation. Embo j. 2020;39(24): e105074.

Publisher's Note